PERGAMON

International Journal of Heat and Mass Transfer 44 (2001) 3775–3785

International Journal of HEAT and MASS TRANSFER

www.elsevier.com/locate/ijhmt

High Schmidt mass transfer in a turbulent impinging slot–jet flow

Radek Chalupa [a], Mingyong Chen [b], Vijay Modi [b,*], Alan C. West [a]

[a] *Department of Chemical Engineering, Columbia University, New York, NY 10027, USA*

[b] *Department of Mechanical Engineering, Columbia University, Mail Code 4703, 500 W. 120th Street, New York, NY 10027, USA*

Received 5 May 2000; received in revised form 10 January 2001

Abstract

High Schmidt number mass transfer to a line electrode in turbulent impinging slot–jet flows is investigated. Slot-based Reynolds numbers from 13 000 to 40 000 are considered. The mass transfer measurements, made by the electrochemical method on 100-micron electrodes, are compared to the computed wall shear via an established analytical relationship. The local shear is estimated from two-dimensional flow-field simulations of the Reynolds averaged Navier–Stokes equations. The k–$\bar{\omega}$ turbulence model [1] was used to calculate the turbulent eddy viscosity, ν_t. The present measurements resolve the sharp variations in mass transfer in the stagnation region. Both the experimental and theoretical results show that the peak values in Nusselt number occur at a point about one jet width away from the stagnation point.

Keywords: Turbulent flow mass transfer; High Schmidt number; Impinging slot–jet; Thin electrode

1. Introduction

Impinging jet systems can achieve high rates of mass transfer. Some industrial-scale electrochemical applications include etching, water rinsing, electroless deposition, and through-mask electrodeposition in the manufacture of electronic and magnetic devices.

Fluid flows encountered in industrial applications are frequently turbulent. In order to accurately capture the unsteady and three-dimensional behavior one would need to use "direct numerical simulation (DNS)" techniques. This approach is rarely carried out except for moderate Reynolds number flows in simple geometries such as for example a fully developed turbulence channel flow [2]. In the present study, the Reynolds averaged Navier–Stokes (RANS) equations are used. In this averaging process, the non-linear terms in the Navier–Stokes equations give rise to parameters that must be modeled. Although many kinds of models have been developed, two-equation models are most popular in engineering applications because of their relative simplicity and the satisfactory results they provide.

Among the large number of two-equation models, the most commonly used are those that solve for the turbulent kinetic energy, k, and either the dissipation rate, ε , or the specific dissipation rate, ω. In the standard high Reynolds number form of the k–ε model the equations are solved only in the region far away from the wall ($y^+ > 30$). The flow in the near-wall region is treated via the "law of the wall". In contrast, for the other models the entire fluid flow field is solved. Polat et al. [3] have reviewed numerical efforts that address turbulent impinging jet flows. Heyerichs and Pollard [4] assessed the k–$\bar{\omega}$ model [1] and various versions of high- and low Reynolds k–ε models by solving the heat transfer problem in turbulent impinging jet flows. Their results show that high Reynolds number k–ε models are not as satisfactory as the low Reynolds number k–ε models and the k–$\bar{\omega}$ model. Chen and Modi [5] calculated the fluid flow and high Schmidt number mass transfer in turbulent impinging slot–jets employing the k–$\bar{\omega}$ model. The mass transfer rate on the impingement plate was compared with the experimental data of

* Corresponding author. Tel.: +1-212-854-2956; fax: +1-212-854-3304.

E-mail address: modi@columbia.edu (V. Modi).

0017-9310/01/$ - see front matter
PII: S0017-9310(01)00042-4

Nomenclature

B	width of the jet (m)
c	concentration of tri-iodide ion (mol m^{-3})
c_∞	bulk concentration of tri-iodide ion (mol m^{-3})
C_f	friction coefficient
$C_\mu, C_{\varepsilon 1}, C_{\varepsilon 2}$	k–ε turbulence model constants
D	diffusion coefficient of tri-iodide ions (m^{-2} s^{-1})
D_t	eddy diffusivity (m^{-2} s^{-1})
f	factor appearing in Eq. 5, $f = \gamma_M L/2\beta_M$
f_μ	k–ε turbulence model damping function
F	Faraday's constant, $F = 96,500$ (C mol^{-1} eq^{-1})
G, G'	turbulent generation (s^{-2})
H	jet-to-plate distance (m)
i_L	limiting current density (A m^{-2})
I	turbulence intensity
k	turbulent kinetic energy (m^{-2} s^{-2})
L	streamwise length of the line sensor (m)
Nu_x	local Nusselt number
Nu	average Nusselt number
p	pressure (N m^{-2})
R_k	k–$\bar{\omega}$ turbulence model constant
R_t	turbulent Reynolds number in k–ε model, $R_t = k^2/v\varepsilon$
R_t^*	turbulent Reynolds number in k–$\bar{\omega}$ model, $R_t^* = k/v\bar{\omega}$
R_w, R_β	k–$\bar{\omega}$ turbulence model constants
Re	Reynolds number, $Re = v_{in}B/v$
Re_y	turbulent Reynolds number in k–ε model, $Re_y = y\sqrt{k}/v$
s	value of x-coordinate at either leading edge or midpoint of sensor (m)
Sc	Schmidt number, $Sc = v/D$
u	velocity component in x-direction (m s^{-1})
v	velocity component in y-direction (m s^{-1})
W	dimension of the channel in z-direction (m)
W_s	dimension of the sensor in z-direction (m)
x	x-coordinate (m)
y	y-coordinate (m)
z	z-direction (m)

Greek symbols

$\bar{\alpha}$	$[((1+f)^{3/2} - (1-f)^{3/2})/f]^{2/3}$
α, α^*	k–$\bar{\omega}$ turbulence model damping functions
$\hat{\alpha}, \hat{\alpha}^*$	k–$\bar{\omega}$ turbulence model constants
β	τ_w/μ (s^{-1})
β^*	k–$\bar{\omega}$ turbulence model damping function
$\Gamma(4/3)$	the gamma function of 4/3, $\Gamma(4/3) = 0.89298$
γ	$\mathrm{d}\beta/\mathrm{d}x$ (m^{-1} s^{-1})
η	similarity transform variable (m)
μ	dynamic viscosity (kg m^{-1} s^{-1})
v	kinematic viscosity (m^2 s^{-1})
v_t	turbulent eddy viscosity (m^2 s^{-1})
ρ	density (kg m^{-3})
τ_w	shear stress on the wall (kg m^{-1} s^{-2})
φ	value of β at either leading edge or midpoint of sensor (s^{-1})
ε	dissipation rate of turbulence kinetic energy (m^2 s^{-3})
σ_k	k–ε turbulence model constant
σ_k^*	k–$\bar{\omega}$ turbulence model constant
σ_ε	k–ε turbulence model constant
$\sigma_{\bar{\omega}}$	k–$\bar{\omega}$ turbulence model constant
$\bar{\omega}$	specific dissipation rate of turbulence kinetic energy (s^{-1})

Subscripts

c	continuously active
i, j	indices for tensor notation
in	nozzle exit
L	mass transfer rate limited
M	midpoint of the sensor
t	turbulent
w	impingement wall
x	local
∞	label for bulk concentration of tri-iodide

Alkire and Ju [6]. Durbin [7] developed a three-equation model (k–ε–v^2), in which there is no "damping function". Behnia et al. [8,9] applied this model and the standard k–ε model to simulate heat transfer in the circular impinging turbulent flow jet. The k–ε–v^2 model prediction of heat transfer coefficient was found to be much better than the standard k–ε model. In the present work, the k–$\bar{\omega}$ [1] will be employed for the numerical simulations.

Flow systems most closely related to the case at hand have been investigated by two other groups, Chin and Agarwal [10] and Alkire and Ju [6]. In both cases electrochemical systems involving continuously active geometries (see [11]) were used and experiments were carried out with slot-width-based Reynolds numbers in the ranges 1000–8000 and 500–2750, respectively.

In the current work, the fluid emerges from a slot nozzle to impinge onto a stationary, submerged plate, as

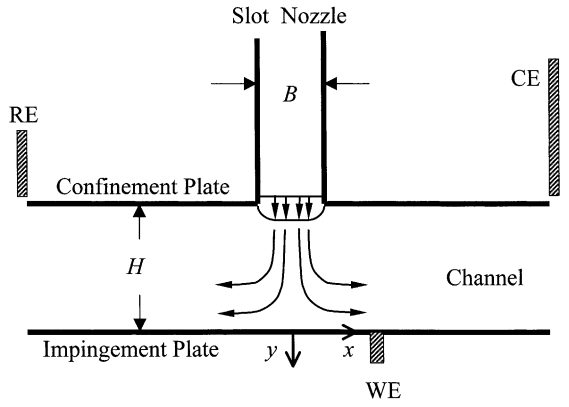

Fig. 1. Schematic diagram of the flow cell. RE, saturated calomel reference electrode; CE, counterelectrode; WE, working electrode.

shown in Fig. 1. Since a plate parallel to the impingement plate is employed, the problem is that of a confined, submerged impingement. The flow can be divided into three spatial regimes: the impingement region, located under the nozzle (i.e., approximately $0 \leqslant x/B < 3$); the transition region, located immediately downstream (i.e., approximately $3 \leqslant x/B < 6$); and channel flow region downstream. The assumed coordinate system is also plotted in Fig. 1. For mass transfer measurements, the impingement plate is insulated except for a thin, rectangular strip (i.e., the mass transfer sensor or the working electrode, WE) on the plate. The concentration on this thin sensor is maintained at a constant value of 0 in accordance with the limiting current condition. The concentration along the upstream section of the impingement plate is set constant to a normalized value of 1. Because the sensor is very thin $(B/35)$ and the Schmidt number of the fluid is very high, it is not necessary to solve the convective mass transfer equation in the entire calculation domain. Instead, boundary layer theory was applied (see [11] for details).

2. Experimental

2.1. Flow cell design

The flow cell was constructed of transparent Plexiglass. The slot nozzle has inner cross-sectional dimensions of $W \times B = 30.3$ mm $\times$ 3.5 mm. The nozzle length is 200 mm, with the last 90 mm being of constant cross-section. The upstream 110 mm has a gradual change in the cross-section from 15 mm $\times$ 15 mm (where the plastic tubing is connected) to the final cross-section of 30.3 mm $\times$ 3.5 mm. Over this length, the mean velocity profile, but not the detailed structure of the turbulent flow, had likely fully developed [12]. The channel part of the flow cell is comprised of two vertical spacers and two plates, with the nozzle being attached to the top plate and the sensor being flush mounted in the bottom one. The lengths of the top and bottom plates are 200.8 and 342.8 mm, respectively, thus allowing the bottom plate to be shifted relative to the top one (permitting the horizontal position of the sensor relative to the nozzle to be adjusted). The dimensions of the cross-section of this channel are $H \times 30.3$ mm, where H can assume values of 3.2, 6.9, and 14.2 mm. A more detailed description of the flow cell's design and operation appears in [11].

The mass transfer sensor (WE or cathode) consisted of 0.1 mm $\times$ 20.3 mm $(= L \times W_s)$ platinum foil, cast in a cylindrical mold. The mold was mounted flush to the center of the bottom plate so that the WE is perpendicular to the flow direction. The counterelectrode (CE) or the anode is a 50 mm $\times$ 300 mm piece of nickel foil and was downstream of the WE mounted on the wall of the container near the outlet of the flow cell. The CE protruded above the liquid level in the tank allowing a simple electrical connection via an alligator clip. The purpose of the CE is to provide an excess surface area (compared to the WE) for the oxidation reaction. Saturated calomel electrode (SCE) was used as a reference (RE) and was positioned near the outlet of the flow cell on the side of the tank opposite to where the CE was located. The purpose of the RE is to provide a fixed potential reference point for the WE, regardless of what is occurring at the CE [13].

The pump used in these experiments was a constant speed centrifugal unit (Baldor Industrial Motor, model 35E74-498, with Sherwood centrifugal pump head, model CMNP34T). The flow rate was controlled by means of a ball valve (Banjo polypropylene ball valve, model VL1001) positioned immediately downstream of the pump and connected to the outlet port of the pump by means of 38.1 mm (1.5 in.) diameter rigid PVC pipe (schedule 40 PVC). A calibrated inline, glass flow meter (Brooks Instrument Division Emerson Electric Company, model 1303AL16BA11A) was used to monitor the flow rate through the system. The connection between the downstream port of the flow meter and the flow cell was made using 12.7 mm (0.5 in.) diameter flexible plastic tubing (Fisherbrand), approximately 1 m in length. The uptake port on the pump was connected to the solution tank using a 38.1 mm (1.5 in.) diameter rigid PVC pipe (schedule 40), with a 0.5 m midsection of this line consisting of a flexible, 38.1 mm (1.5 in.) diameter, metal-spiral-reinforced rubber hose (to dampen out the effects of vibration of the pump motor on the experimental setup). Flow rates ranging from about 300–1000 $cm^3\ s^{-1}$ were used.

To counteract the significant heating of the solution (from room temperature to approximately 60°C in a course of about 1 h) observed during the initial trial runs (due to both the heat dissipated by the pump motor as

well as by the major pressure drops within the flow line), a cooling system was placed inside the solution tank. The cooling system consisted of approximately 2 m of thin-walled, flexible plastic tubing (12.7 mm or 0.5 in. diameter with wall thickness of 2.4 mm or 3/32 in.) coiled up into a helix, approximately 20 cm in diameter. Cool tap water (19 ± 1°C) was circulated continuously through the cooling coils during the experiments. With this cooling system in place, the temperature of the solution did not exceed 27°C.

2.2. Solution chemistry and measurement procedure

Experiments used 30 l of electrolyte composed of 0.0005 M iodine and 0.10 M potassium iodide (where approximately 8 l were used for initial rinsing of the flow system). Reduction of tri-iodide ion takes place at the sensor. The system's temperature was maintained at 26 ± 1°C. The diffusivity of the tri-iodide ion (at the corresponding temperature) was measured to be $D = 1.01 \times 10^{-5}$ cm^2 s^{-1} (using the rotating disc method). The kinematic viscosity of the solution was estimated using tabulated values for liquid water (temperature effect corrections) and aqueous solutions of potassium iodide (concentration effect corrections) to be $\nu = 0.84$ cm^2 s^{-1}. The flow rates were monitored using an inline flow meter. The measured flow rates and the corresponding uncertainties (obtained by repeating the calibration twice) were as follows: 440 ± 5 cm^3 s^{-1} ($Re = 13300 \pm 200$); 610 ± 10 cm^3 s^{-1} ($Re = 23900 \pm 300$); and 1000 ± 30 cm^3 s^{-1} ($Re = 39000 \pm 1000$). The corresponding numerical simulations were carried out for Reynolds number values of 14 000, 25 000, and 40 000, respectively. To simplify the notation, the experimental data are also labeled by these "rounded-off" Reynolds number values.

Prior to pumping the electrolyte into the system, the inside of the flow cell and the anode were first rinsed with 200 proof ethanol. Following this step, the system was thoroughly rinsed with deionized water several times and allowed to air dry. The system was then rinsed with approximately 8 l of the 30-l solution batch, before the introduction of the remaining 22 l. Measurements were taken after about 5 s of a constant volumetric flow rate. A Pine Instruments AFRDE4 potentiostat was used to control potential and measure current (i.e., the mass transfer limited current density, i_L). The potential was set at the limiting current plateau, specifically at an overpotential of -0.40 V vs. the calomel RE. In addition, two Hewlett Packard 34401A multimeters were used, one for displaying the potential setting and the other for displaying the current and interfacing with the data acquisition software (Hewlett Packard 34812A BenchLink/Meter, version 1.0). The existence of mass transfer limited current at the above potential setting was confirmed by linear-sweep voltammetry for each vertical spacer and at two horizontal sensor locations, i.e., $x/B = 1$ and 20.

It was estimated that each adjustment of the sensor in the horizontal direction carried an uncertainty of ± 0.5 mm. Experiments were repeated at least twice (each time with a fresh batch of solution) to check for reproducibility.

3. Fluid flow

To obtain the local shear on the impingement wall, two-dimensional steady-state Reynolds-averaged-Navier–Stokes (RANS) equations are solved with the k–$\bar{\omega}$ turbulence model [1]. The steady-state continuity and RANS equations shown below were solved in the entire fluid flow domain:

$$\frac{\partial u_i}{\partial x_i} = 0, \tag{1}$$

$$\frac{\partial (u_i u_j)}{\partial x_j} = -\frac{1}{\rho}\frac{\partial p}{\partial x_i} + \frac{\partial}{\partial x_j}\left[(\nu + \nu_t)\left(\frac{\partial u_i}{\partial x_j} + \frac{\partial u_j}{\partial x_i}\right)\right]. \tag{2}$$

The details of the turbulence model utilized to obtain the turbulent eddy viscosity, ν_t, are shown in Appendix A.

The boundary conditions were specified as follows. At the nozzle exit, a uniform velocity profile was assumed. No-slip velocity conditions were imposed at the impingement and confinement walls. At the symmetry boundary (i.e., $x/B = 0$), standard symmetry conditions were imposed on all the variables (i.e., u, v, p, k, and $\bar{\omega}$). At the outlet boundary, the pressure was set equal to the atmospheric pressure and the first derivatives of the other variables along the streamwise direction were assumed to vanish. At all other boundaries, pressure was extrapolated from the interior of the domain with a zero second derivative on the boundary. The suitability of this computational pressure boundary condition for internal flow over has been shown in [14]. The distribution of k and $\bar{\omega}$ at the nozzle exit was approximated from the turbulence intensity, I, and a characteristic length, L, of the jet flow: $k = 3/2(Iv_{in})^2$, $\bar{\omega} = k/0.015B$. At the no-slip wall, the kinetic energy is set to 0, but there is no obvious choice of boundary conditions for the quantity ω. In the simulation, the boundary value of ω was specified at the near-wall cell according to the formula, $\omega = 6\nu/(\beta y^2)$, where y is the normal distance from the cell center to the wall [1]. The mesh size was chosen so that the value of y^+ for the near-wall cell is less than 2.5.

For the simulation using the k–$\bar{\omega}$ model, a cell-centered finite volume approach based on the artificial compressibility method was employed in solving the velocity field. Details of the computational approach are given in [14]. Once the flow field was obtained, the wall shear stress is computed using $\tau_w = \mu \partial u/\partial y$ and converted into a friction coefficient, $C_f = 2\mu\beta/\rho v_{in}^2$, where $\beta = \tau_w/\mu$.

4. Mass transfer

In the present paper, the active mass transfer region was a very thin strip on the impingement plate ($L/B = 0.03$) assumed to be centered at $x = x_M$. Thus, in order to avoid resolution problems near the thin strip, boundary layer theory was applied to solve the two-dimensional convective diffusion equation. With the assumption that forced convection dominates over diffusion in the flow direction (the x-direction), the equation simplifies to:

$$u\frac{\partial c}{\partial x} + v\frac{\partial c}{\partial y} = \frac{\partial}{\partial y}\left((D + D^{(t)})\frac{\partial c}{\partial y}\right). \tag{3}$$

The two velocity components in the above equation, u and v, are assumed to have the forms:

$$u = y\beta(x) \quad \text{and} \quad v = -\frac{1}{2}y^2\gamma(x), \tag{4}$$

where

$$\beta(x) = \left.\frac{\partial u}{\partial y}\right|_{y=0} \quad \text{and} \quad \gamma(x) = \frac{\mathrm{d}\beta}{\mathrm{d}x}.$$

Son and Hanratty [15] and Shaw et al. [16] conducted studies of turbulent mass transfer to electrodes of various lengths ($20 < L^+ < 10\,000$) at large Schmidt number ($Sc = 2400$) for fully developed pipe flow and found that turbulent eddy diffusivity term, $D^{(t)}$, is negligible compared to the molecular diffusivity, D, whenever the condition, $\sqrt{\beta/\nu}L \equiv L^+ < 700$, is satisfied. In the present study, L^+ did not exceed 100. Hence, the turbulent eddy diffusivity, $D^{(t)}$ can be omitted from Eq. (3), reducing the problem to the same as that under laminar flow conditions. A detailed analysis of the laminar flow problem, i.e., Eq. (3) in the absence of $D^{(t)}$, was presented in our earlier paper [11]. From this analysis it is possible to express the Nusselt number (away from stagnation point) in terms of the friction coefficient, C_f, (obtained from fluid dynamic computations and evaluated at the sensor's midpoint, x_M), via the relationship:

$$Nu = \frac{1}{L}\int_{x_M - L/2}^{x_M + L/2} Nu_x \,\mathrm{d}x = 0.308\,\bar{\alpha}(B/L)^{1/3}Sc^{1/3}C_f^{1/3}Re^{2/3}, \tag{5}$$

where

$$Nu_x = \left(\frac{B}{c_\infty}\right)\left.\frac{\partial c(x,y)}{\partial y}\right|_{y=0},$$

$$\bar{\alpha} = \left[\frac{(1+f)^{3/2} - (1-f)^{3/2}}{f}\right]^{2/3} \quad \text{and} \quad f = \frac{\gamma_M L}{2\beta_M}.$$

For a pure shear flow $f = 0$ and $\alpha = 3^{2/3}$. Furthermore, according to Kakac et al. [17], the friction factor in a pure shear flow can be related to Reynolds number through:

$$C_f = \frac{0.0317}{Re^{0.3}(H/B)^2}. \tag{6}$$

At the stagnation point, β_M, goes to 0. Hence,

$$Nu = \frac{B}{6^{1/3}\Gamma(4/3)}Sc^{1/3}\left(\frac{\gamma_M}{\nu}\right)^{1/3}. \tag{7}$$

Experimental mass transfer data can be compared with the results from Eqs. (5) and (7) by converting the limiting current density values, i_L, into Nusselt numbers (using Faraday's law) through:

$$Nu = \frac{Bi_L}{DFc_\infty}. \tag{8}$$

5. Results and discussion

5.1. Mesh independence and validation of turbulence models

In numerically simulating the fluid flow field, the length of the domain in the streamwise direction was chosen such that the results were not altered by any further extension of the streamwise domain size. The turbulence intensity at the jet exit was set to 4% except where otherwise specified. Non-uniform grids were used with the dimensionless distance in wall units (i.e., y^+) from the center of the near-wall cell to the wall being less than 2.5. The stretching factor was not allowed to exceed 1.1. Fig. 2 shows the variation of Nusselt number with x/B obtained for two different meshes using the k–$\bar{\omega}$ model. The results do not show any appreciable difference due to grid size. For all subsequent simulations a grid size of 100×100 was used unless otherwise indicated.

To further ensure the validity of the numerical solver, simulations were compared to experimental data [18] for the case of heat transfer from a slot–jet impinging on a wall. The parameter values chosen for the comparison were: $Re = 11\,000$, $H/B = 5$, $I = 2.5\%$, and $Pr = 0.72$. In that experimental study, the entire impingement plate was heated (a setup which has previously been referred to by Chen et al. [11] as a "continuously active geometry"). The local data were acquired by segmenting the impingement plate into sections of finite length, with the smallest section ($0.6B$ in size) being near the stagnation point. The simulation results and the experimental data shown in Fig. 3 are in very good agreement near the stagnation point $x/B = 0$) and in the wall jet region. The secondary peak in Nu_c (in the region $4 \leqslant x/B \leqslant 7$) is more pronounced and slightly further upstream in the numerical simulation.

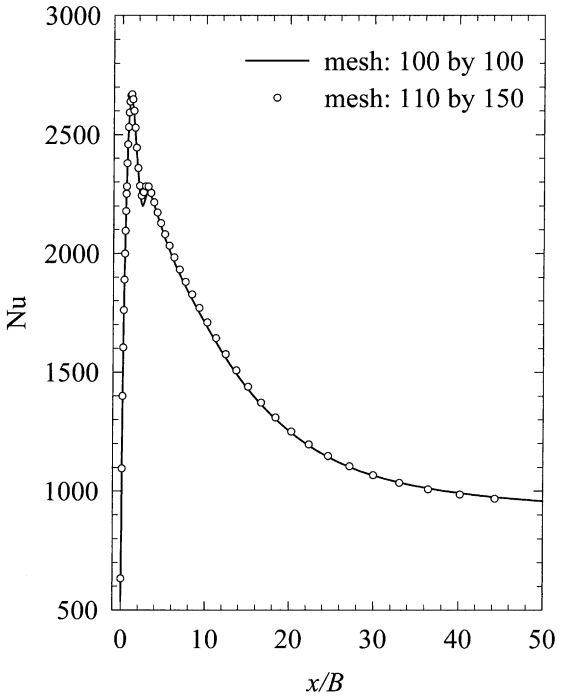

Fig. 2. Mesh independence test of the k–$\bar{\omega}$ model ($H/B = 2$, $Re = 14\,000$, $Sc = 804$).

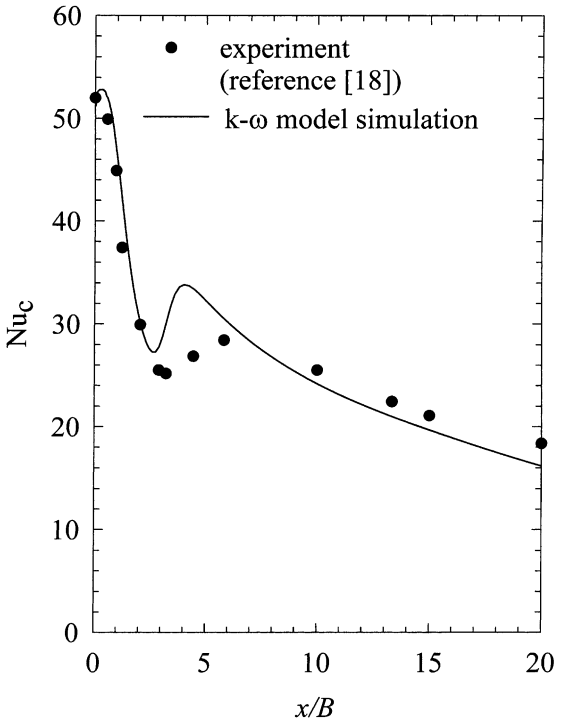

Fig. 3. Comparison of numerical results to experimental data of heat transfer coefficient, Nu_c, on a continuous heated impingement wall ($H/B = 5$, $Re = 11\,000$, $Pr = 0.72$).

5.2. Computed and experimental results

Fig. 4 shows the variation of experimentally measured mass transfer rate (as indicated by both the white-filled data points to the right of stagnation point and black-filled data points to the left), Nu, with respect to x/B about the stagnation point ($x/B = 0$) in the region $-5 \leqslant x/B < 5$. The vertical error bars represent estimates of the uncertainty in the experimentally measured mass transfer rates at given distances away from the stagnation point. The horizontal error bars in this figure are estimates of the uncertainty in the horizontal positioning of the sensor. It was assumed that this uncertainty is independent of the particular x/B setting and is equal to about ± 0.5 mm$/B = \pm 0.1$. The dotted line in the region $x/B > 0$ simply connects the white-filled data points with straight line segments. This same line has been reflected about the axis $x/B = 0$ into the region $x/B < 0$ to demonstrate that the experimentally acquired data exhibit symmetry about the stagnation point to within experimental uncertainty. This serves as a check that the observed displacement of the peak in Nusselt number values away from the jet's stagnation point is real.

Experimental data, showing the variation of mass transfer rate, Nu, with x/B were acquired for three dif-

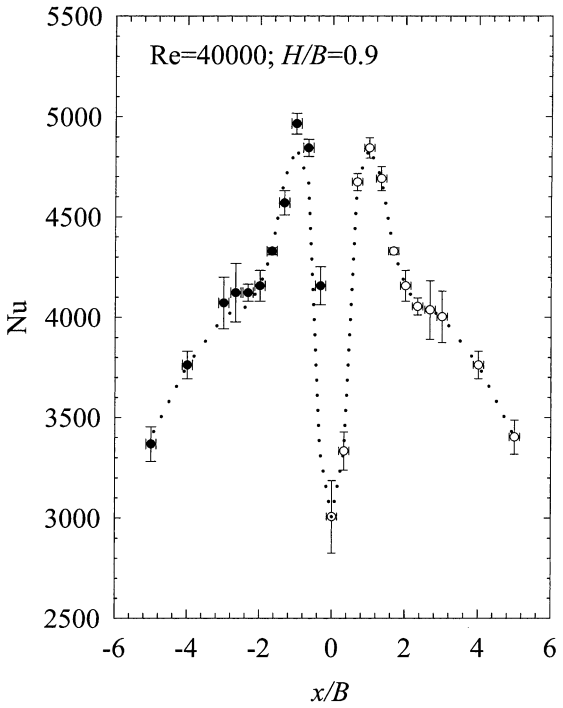

Fig. 4. Experimentally measured variation of Nu with x/B about the stagnation point, $x/B = 0$ (dotted line and symbols both correspond to experimentally acquired data).

ferent flow rates and for three different nozzle-to-plate (H/B) distances, as shown in Figs. 5–7. The corresponding numerical simulation results of Nusselt number (thin lines) in the three figures were obtained from Eqs. (5) and (7), where the variables β_M and γ_M were computed using the flow solver. The thicker lines in these three figures (at $15 \leqslant x/B \leqslant 20$) represent the fully developed mass transfer rates (obtained using Eqs. (5) and (6)), which according to simulations should occur further downstream.

Both experiments and simulations show that the mass transfer rate increases sharply from $x/B = 0$, the stagnation point, to about $x/B = 1$, where the primary peak in Nu values occurs. Proceeding further downstream, the Nusselt numbers drop quickly and approach constant values corresponding to those in fully developed, channel flows. Note that the behavior in the stagnation region is different from the results of both Gardon and Akfirat [18], as well as Alkire and Ju [6], which were acquired with continuously active geometries. The spatial variation of turbulent mass transfer rate qualitatively resembles that in laminar jet flow [11].

The numerical results of mass transfer rate at the stagnation point (obtained from Eq. (7) are much lower than experimental data for all flow rates and H/B cases studied. Eq. (7)) shows that Nusselt number at the stagnation point is directly proportional to $\gamma^{1/3}$. Since

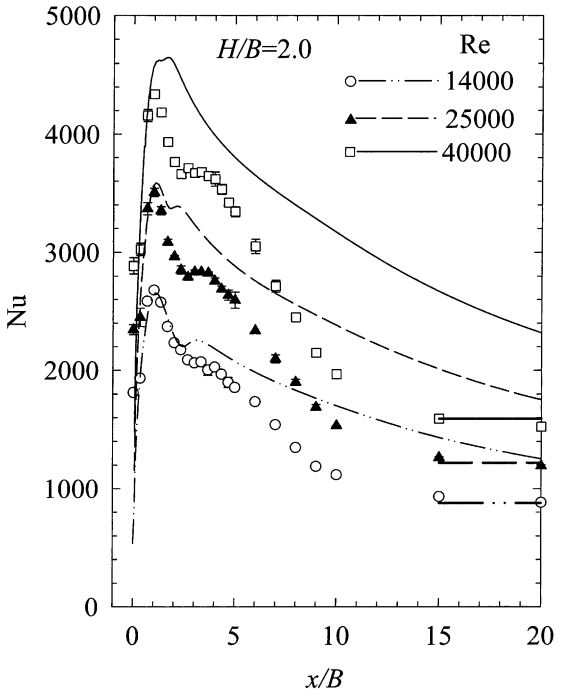

Fig. 6. Variation of Nu with x/B for $H/B = 2.0$ (thin lines: simulation; thick lines: channel flow solutions; symbols: experiments).

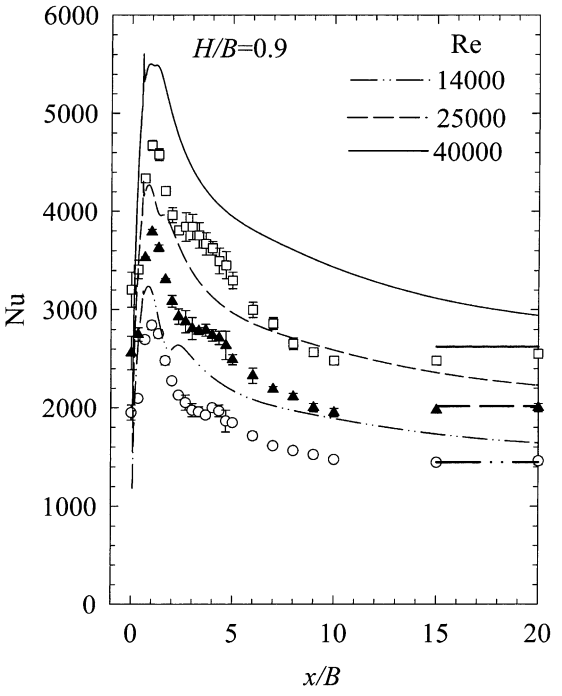

Fig. 5. Variation of Nu with x/B for $H/B = 0.9$ (thin lines: simulation; thick lines: channel flow solutions; symbols: experiments).

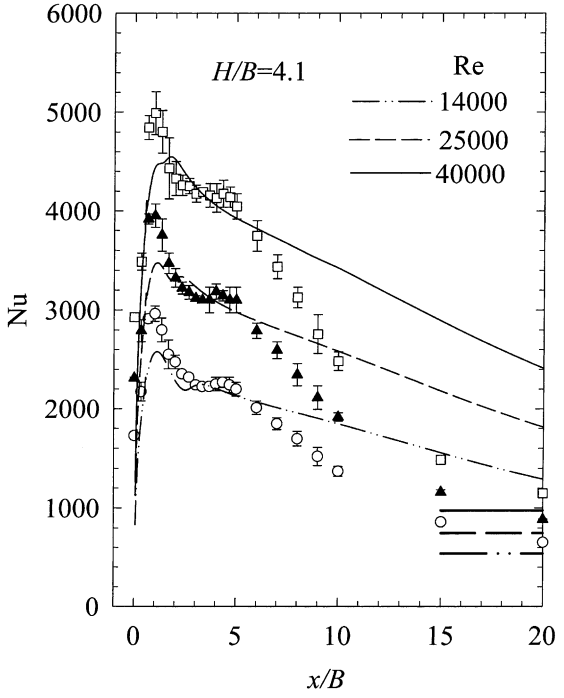

Fig. 7. Variation of Nu with x/B for $H/B = 4.1$ (thin lines: simulation; thick lines: channel flow solutions; symbols: experiments).

the mass transfer coefficient increases very rapidly immediately downstream of the stagnation point, the value of γ could be extremely large in this region. Under these circumstances, both simulations and experiments can easily introduce error. In the case of the experiments, any small departure of the line sensor from the stagnation point (due to inaccuracies in the horizontal positioning) would cause a sharp increase in Nusselt number.

It can be seen that the experimental mass transfer rates are lower and achieve fully developed values further upstream than the simulation results would predict. One possible reason for this discrepancy could be the presence of a large recirculation region near the confinement wall as shown in Fig. 8. The streamline plot in this figure is obtained from simulations for $H/B = 2$ and $Re = 40\,000$. The recirculation region is seen to extend as far downstream as $x/B = 10$. A two-equation turbulence model used in the present paper may not be able to fully capture the effects of this recirculation region.

Theoretical results of peak and fully developed mass transfer rates for different Reynolds numbers and nozzle-to-plate distances are compared in Fig. 9 to the experiments. For both experiments and simulations, the peak and the fully developed Nusselt numbers increase with Reynolds number. The computed peak mass transfer rate decreases with nozzle-to-plate distances for all three values of the Reynolds number studied. The experimental peak value, however, first drops from $H/B = 1$ to 2 and then rises as H/B increases from 2 to 4. These variations with H/B are however small and experimental peak mass transfer rates lie within the variation suggested by the simulations. The experimental mass transfer rates at $x/B = 20$ (the maximum x/B setting in the experiments) are in very good agreement with the predicted fully developed Nusselt numbers for $H/B = 1$ and 2. This indicates that fully developed conditions are reached within $x/B = 20$ for $H/B \leqslant 2$, in the experiments. The agreement is not as good for $H/B = 4$, suggesting that fully developed conditions are not attained for $H/B \geqslant 4$ within $x/B = 20$.

5.3. Discussion

It is seen in Figs. 5–7 that the computational mass transfer rates are consistently higher than the experimental data especially in the region $x/B > 5$. In order to determine whether this discrepancy is due to the choice of a particular turbulence model, the same problem was also treated using a low Reynolds number k–ε model [19] with the help of a commercial CFD software package, *STAR-CD*. The model equations and constants are written in detail in Appendix A. The results are compared with the k–$\bar{\omega}$ model results and experimental data in Fig. 10 for the case of $H/B = 2$, $Re = 14\,000$. As is apparent in this figure, both models lead to similar results. The agreement with the experimental data is best in the impingement and transition regions

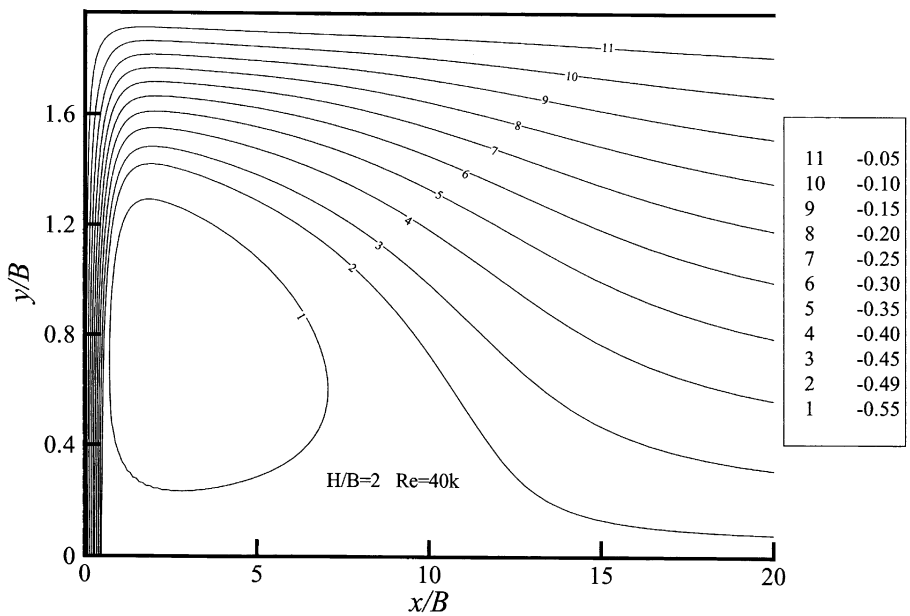

Fig. 8. Streamlines in turbulent impinging jet flow. Since the symmetric half of the flow is computed, the stream function at the confinement wall is −0.50. The stream function at the symmetry boundary, $x/B = 0$, and at the impingement plate, $y/B = 2.0$, has been set to 0.0.

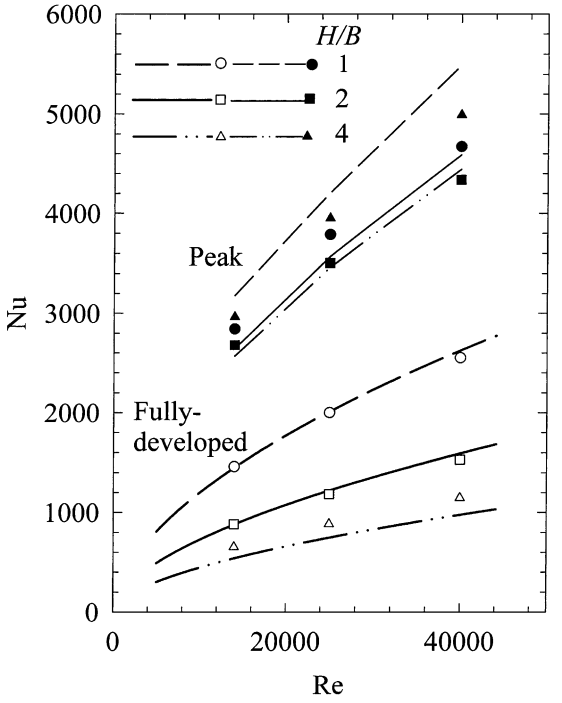

Fig. 9. Comparison of theoretical to experimental *Nu* at $x/B = 1$ and fully developed region (symbols: experiments; lines: simulations).

(i.e., approximately $x/B < 5$). For $x/B > 5$ the experimental mass transfer drops off to its fully developed values at a much faster rate than the simulations.

Heyerichs and Pollard [4] simulated turbulent slot–jet flow using several different turbulence models for the case $H/B = 2.6$ and $Re = 10000$. They obtained the friction coefficient, C_f, along the impingement plate (Fig. 8 in the reference). These results of friction coefficient are converted in the present paper into mass transfer rate coefficients, *Nu*, using Eqs. (5)–(7) and plotted in Fig. 11 by means of two solid curves. These two solid curves represent the upper and lower bounds of Nusselt number values along the plate from seven different two-equation models. The results from high Reynolds number models that utilize wall functions are excluded. The simulation results obtained in the present study (shown for clarity in Fig. 10 but not in Fig. 11) lie within these two curves as well. The experimental data for $H/B = 2.0$ and $Re = 14000$ are also plotted in Fig. 11. It can be seen that the turbulence models consistently predict the same sharp rise in Nusselt number in the stagnation region and the same primary peak in Nusselt number (at about $x/B = 1$). The largest scatter due to use of different turbulence models occurs in the region $3 < x/B < 10$, where the simulations indicate the presence of a recirculation region. Experimental results lie within the upper and lower bounds of the turbulence

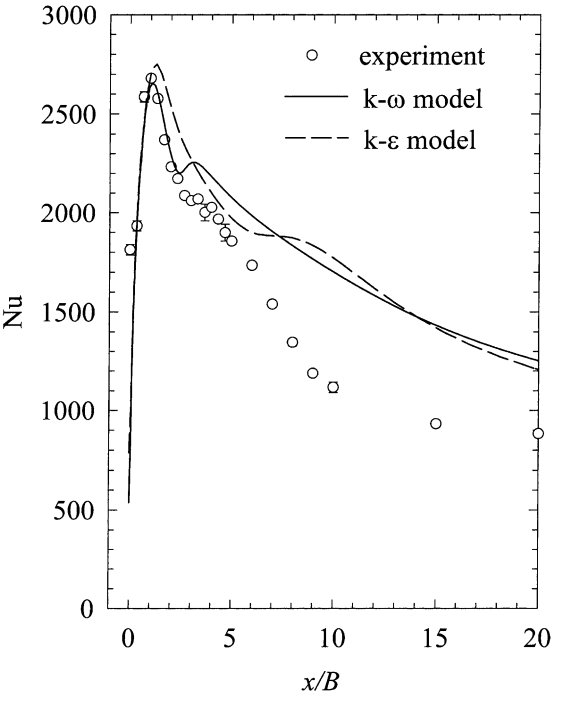

Fig. 10. Comparison of numerical mass transfer coefficients from k–$\bar{\omega}$ and k–ε models to experimental data ($H/B = 2$, $Re = 14000$, $Sc = 804$).

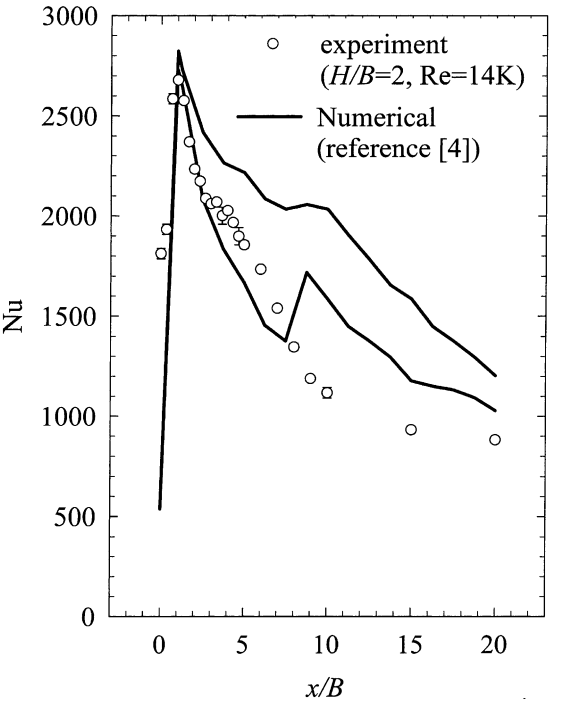

Fig. 11. Evaluation of the range of numerical mass transfer coefficients from different turbulence models (symbols: $H/B = 2$, $Re = 14000$; lines: $H/B = 2.6$, $Re = 10000$).

models for $x/B \leqslant 7$. Further downstream, for $x/B > 10$, the scatter in the turbulence model reduces but the experimental Nusselt number values are consistently lower than the numerical simulations shown in Fig. 11 would predict.

6. Conclusions

Mass transfer to a flush-mounted, line electrode from a submerged, confined, turbulent flow, slot, impinging jet is examined. Both numerical and experimental investigations of this flow system clearly capture the fact that the peak in the mass transfer rate does not occur directly under the slot nozzle. This peak in the Nusselt number is instead displaced about one nozzle width away from the stagnation point. The numerical results of peak and fully developed Nusselt number are in fair agreement with the experimental data (as shown in Fig. 9). The experimental Nusselt numbers, however, diminish to their fully developed channel flow values more quickly (i.e., at lower x/B settings) than the corresponding numerical results.

Small streamwise electrode size ($L \ll B$) or a very fine segmentation of the active surface in a continuously active geometry system is essential if one is to observe the peak in the mass transfer rate away from the stagnation point. Furthermore, the thin electrode method of mass transfer rate measurement is more sensitive to the wall shear stress than the continuously active geometry method, making thin, isolated electrodes better experimental tools for the validation of fluid dynamics computations.

Acknowledgements

This work was supported by the National Science Foundation under award number CTS-97-06824.

Appendix A

There are two different RANS turbulence models that are used in this study. The equations and model parameters for the k–$\bar{\omega}$ model [1] with turbulent kinetic energy, k, and specific dissipation rate, $\bar{\omega}$, are:

$$\frac{\partial(u_i k)}{\partial x_i} = \frac{\partial}{\partial x_i}\left[(\nu + \sigma_k^* \nu_t)\frac{\partial k}{\partial x_i}\right] + \nu_t G - \beta^* \bar{\omega} k, \tag{A.1}$$

$$\frac{\partial(u_i \bar{\omega})}{\partial x_i} = \frac{\partial}{\partial x_i}\left[(\nu + \sigma_{\bar{\omega}} \nu_t)\frac{\partial \bar{\omega}}{\partial x_i}\right] + \alpha \nu_t G \frac{\bar{\omega}}{k} - \beta \bar{\omega}^2. \tag{A.2}$$

These equations are used to obtain the turbulent eddy viscosity in Eq. (2) from

$$\nu_t = \alpha^* \frac{k}{\bar{\omega}}. \tag{A.3}$$

Table 1

G	$\left(\frac{\partial u_i}{\partial x_j} + \frac{\partial u_j}{\partial x_i}\right)\frac{\partial u_i}{\partial x_j}$
α	$\frac{5}{9}\frac{\hat{\alpha} + R_t^*/R_w}{1 + R_t^*/R_w}(\alpha^*)^{-1}$
R_t^*	$k/\bar{\omega}\nu$
α^*	$\frac{\hat{\alpha}^* + R_t^*/R_k}{1 + R_t^*/R_k}$
β^*	$\frac{9}{100}\frac{5/18 + (R_t^*/R_\beta)^4}{1 + (R_t^*/R_\beta)^4}$

The quantity G and damping functions are listed in Table 1.

The model constants and parameters appearing in the k–$\bar{\omega}$ model are: $\sigma_k^* = 1/2$, $\sigma_\omega = 1/2$, $\beta = 3/40$, $\hat{\alpha}^* = \beta/3$, $R_\beta = 8$, $R_k = 6$, $R_w = 2.7$, and $\hat{\alpha} = 1/10$.

The other RANS model utilized is a low Reynolds number incompressible k–ε model [19]. The constitutive equations for the k–ε model are:

$$\frac{\partial(u_i k)}{\partial x_i} = \frac{\partial}{\partial x_i}\left(\frac{\nu + \nu_t}{\sigma_k}\frac{\partial k}{\partial x_i}\right) + \nu_t G - \varepsilon,$$

$$\frac{\partial(u_i \varepsilon)}{\partial x_i} = \frac{\partial}{\partial x_i}\left(\frac{\nu + \nu_t}{\sigma_\varepsilon}\frac{\partial \varepsilon}{\partial x_i}\right) + C_{\varepsilon 1}\nu_t(G + G')\frac{\varepsilon}{k} - C_{\varepsilon 2} f_1 \frac{\varepsilon^2}{k}, \tag{A.4}$$

The above equations are used to determine the turbulent eddy viscosity ν_t in Eq. (2) from

$$\nu_t = f_\mu \frac{C_\mu k^2}{\varepsilon}. \tag{A.5}$$

The expression of G is the same as in the k–$\bar{\omega}$ model. The quantities G' and the damping functions used in the k–ε model are shown in Table 2.

The numerical values of the constants appearing above are: $C_\mu = 0.09$, $\sigma_k = 1.0$, $\sigma_\varepsilon = 1.22$, $C_{\varepsilon 1} = 1.44$, and $C_{\varepsilon 2} = 1.92$.

Table 2

G'	$1.33 f_1 \left[G + 2\nu\frac{k}{y^2}\right] e^{-0.00375\, Re_y^2}$
f_1	$1 - 0.3e^{-R_t^2}$
R_t	$k^2/\nu\varepsilon$
f_μ	$[1 - e^{-0.0198\, Re_y}]\left(1 + \frac{5.29}{Re_y}\right)$
Re_y	$y\sqrt{k}/\nu$

References

[1] D.C. Wilcox, Turbulence Modeling for CFD, second ed., DCW Industries, La Canada, CA, 1994, pp. 87, 148–152, 276–277.

[2] J. Kim, P. Moin, R. Moser, Turbulence statistics in fully developed turbulent channel flow at low Reynolds number, J. Fluid Mech. 177 (1987) 133–166.

[3] S. Polat, B. Huang, A.S. Mujumdar, W.J.M. Dougas, Numerical flow and heat transfer under impinging jets: a review, in: C.L. Tien, T.C. Chawla (Eds.), Annual Reviews of Numerical Fluid Mechanics and Heat Transfer, vol. 1, Hemisphere, New York, 1989, pp. 157–197.

[4] K. Heyerichs, A. Pollard, Heat transfer in separated and impinging turbulent flows, Int. J. Heat Mass Transfer 39 (1996) 2385–2400.

[5] Q. Chen, V. Modi, Mass transfer in turbulent impinging slot jets, Int. J. Heat Mass Transfer 42 (1999) 873–887.

[6] R. Alkire, J. Ju, High speed selective electroplating with impinging two-dimensional slot jet flow, J. Electrochem. Soc. 134 (2) (1987) 294–299.

[7] P.A. Durbin, Near-wall turbulence closure modeling without "damping functions", Theoret. Comput. Fluid Dyn. 3 (1991) 1–13.

[8] M. Behnia, S. Parneix, P. Durbin, Simulation of jet impingement heat transfer with the k–ε–v^2 model, Center Turbulence Research Annual Research Briefs, 1996, pp. 3–16.

[9] M. Behnia, S. Parneix, P. Durbin, Accurate modeling of impinging jet heat transfer, Center Turbulence Research Annual Research Briefs, 1997, pp. 149–164.

[10] D.-T. Chin, M. Agarwal, Mass transfer from an oblique impinging slot jet, J. Electrochem. Soc. 138 (9) (1991) 2643–2650.

[11] M. Chen, R. Chalupa, A.C. West, V. Modi, High Schmidt mass transfer in a laminar impinging slot jet flow, Int. J. Heat Mass Transfer 43 (2000) 3907–3915.

[12] M.C. Potter, D.C. Wiggert, Mechanics of Fluids, second ed., Prentice-Hall, Upper Saddle River, NJ, 1997, pp. 260–261.

[13] A.J. Bard, L.R. Faulkner, Electrochemical Methods, Wiley, New York, 1980, p. 3.

[14] H. Cabuk, C.-H. Sung, V. Modi, Explicit Runge–Kutta method for three-dimensional internal incompressible flows, AIAA J. 30 (8) (1992) 2024–2031.

[15] J.S. Son, T.J. Hanratty, Limiting relation for the eddy diffusivity close to a wall, AIChE J. 13 (4) (1967) 689–696.

[16] P.V. Shaw, L.P. Reiss, T.J. Hanratty, Rates of turbulent transfer to a pipe wall in the mass transfer entry region, AIChE J. 9 (3) (1963) 362–364.

[17] S. Kakac, R.K. Shah, W. Aung, Handbook of Single-Phase Convective Heat Transfer, Wiley, New York, 1987, p. 4.62.

[18] R. Gardon, J.C. Akfirat, Heat transfer characteristics of impinging two-dimensional air jets, ASME J. Heat Transfer 101 (1966) 101–108.

[19] F.S. Lien, W.L. Chen, M.A. Leschziner, Low-Reynolds-number eddy-viscosity modelling based on non-linear stress–strain/vorticity relations, in: W. Rodi, G. Bergeles (Eds.), in: Proceedings of the 3rd Symp. on Engineering Turbulence Modeling and Measurements, Crete, Greece, Elsevier Science, Amsterdam, 1996, pp. 91–100.